Chemical Science

ROYAL SOCIETY OF CHEMISTRY

EDGE ARTICLE

View Article Online
View Journal | View Issue

Cite this: *Chem. Sci.*, 2025, **16**, 11498

All publication charges for this article have been paid for by the Royal Society of Chemistry

Site-selective ligand defects open up a Zr-oxo cluster electron transfer pathway for CO_2 photoreduction†

Yuhang Qi,[a] Yiqiang He,[b] Yuxin Liu,[a] Zhe Zhang,[a] Chunguang Li,[a] Fanchao Meng,[c] Shiyu Wang,[c] Xiaobo Chen,[d] Zhan Shi *[a] and Shouhua Feng[a]

Received 15th February 2025
Accepted 15th May 2025

DOI: 10.1039/d5sc01194a

rsc.li/chemical-science

Whilst defect engineering is a sound approach to enhance CO_2 photoreduction based on metal organic frameworks (MOFs), the underlying mechanisms were not well understood on an atomic scale. This study aims to elucidate the mechanisms at the atomic level, to provide vital insights to enable the design and development of selectively introduced ligand defects to maximize the CO_2 photoreduction capability of a classical MOF UiO-66–NH_2 without the need for co-catalysts, sacrificial agents and photosensitizers. Defect-containing UiO-66–NH_2 (Zr/$Ce_{0.25}$) demonstrates superior charge separation and CO_2 photoreduction than both regular UiO-66–NH_2 (Zr/$Ce_{0.25}$) and UiO-66–NH_2. The doped Ce is a key contributor to managing the coordination environment of the linkers, enabling the formation of selectively introduced ligand defects. The selective loss of ligands exposes pyramid-shaped activated clusters and facilitates spatial charge separation. As a result, electrons are transferred through Ce–O–Zr and Ce–$O_{vacancy}$–Zr pathways, effectively narrowing the band gap and suppressing photoinduced charge recombination. These findings are expected to provide alternative perspectives on selective defect engineering for the design and manufacture of high-performance MOF photo-catalysts for a variety of value-added engineering applications.

Introduction

Photocatalysis offers an effective approach to convert CO_2 into value-added products such as fuels, presenting a promising solution to both climate change and fossil fuel shortages.[1] Given the definite and tunable composition and structure of metal–organic frameworks (MOFs), it is possible to draw a connection between their structures and properties.[2] The applicability of MOFs in photocatalysis has been demonstrated and the photocatalytic mechanisms by which they function have been illuminated through the precise tuning of MOF structures.[3–5]

MOFs are promising candidates with excellent photocatalytic performance due to their high specific surface area available for absorption, their numerous active metal sites for activating intermediates, and their tunable ligands for photoabsorption and electron injection.[6–9] However, MOFs show a strong dependence on co-catalysts, sacrificial agents or even photosensitizers, indicating that the full potential of MOFs for photocatalysis is yet to be discovered.[10–12] As such, there is a pressing need to figure out feasible approaches to develop the desired intrinsic properties of MOFs, such as *via* defect engineering, to maximize the catalytic functions of MOFs.[13–16]

Defect engineering refers to the introduction of incongruous units into a perfect crystalline structure to disrupt its long-range order either in metals (or clusters) or ligands.[17] Defect engineering improves the photocatalytic performance on many levels, such as by expanding the pore volume, tuning the band gap and creating active sites.[18–21] However, there are few reports on accelerating the charge separation in MOFs *via* defect engineering.[22–24]

Given that classical defect engineering is a random loss of metal/clusters or linkers without selectivity, it is challenging to tailor the coordination environment within MOFs to build a desired electron transfer pathway. A series of mixed-ligand (terephthalic acid and amino terephthalic acid) MIL-125 MOFs were prepared to determine the mechanistic roles of various ligands in creating selective defects and imparting relevant photoactive performance.[25] In comparison with terephthalic acid, amino terephthalic acid is thermally labile, which leads to uniform ligand deficiencies. Such a concept inspired us to investigate if the physical and chemical

[a]*State Key Laboratory of Inorganic Synthesis and Preparative Chemistry, College of Chemistry, Jilin University, Changchun 130012, China. E-mail: zshi@mail.jlu.edu.cn*
[b]*College of Chemistry and Chemical Engineering, Jiangxi Normal University, Nanchang 330022, China*
[c]*Key Laboratory of High Performance Plastics, Ministry of Education, College of Chemistry, Jilin University, Changchun 130012, China*
[d]*School of Engineering, RMIT University, Carlton, VIC, 3053, Australia*

† Electronic supplementary information (ESI) available. See DOI: https://doi.org/10.1039/d5sc01194a

differences between various parts of a catalyst can be utilized to introduce selective linker defects.

Herein, we employ a thermally induced strategy to create MOFs with site-selective ligand defects. We selected Ce-doped UiO-66–NH_2 as the matrix and leveraged the differences in coordination environments to introduce defects. When Ce is doped into Zr-oxo clusters, their coordination environments are changed and the linkers coordinated to Ce are located at thermally labile sites. Extended X-ray absorption fine structure (EXAFS) analysis confirms the existence of selective ligand deficiencies and unsymmetrical pyramid clusters. X-ray photoelectron spectroscopy (XPS) demonstrates that the defects open up an additional electron transfer pathway between the Ce and Zr to facilitate charge transfer. Density-functional theory (DFT) calculations further support the origin of the selectively introduced defects and the photocatalysis mechanisms. This work is expected to provide alternative guidance to optimize MOFs coordination environments through selective defect engineering strategies.

Results and discussion

Structural characteristics

D-UiO-66–NH_2 ($Zr/Ce_{0.25}$) was prepared *via* a two-step process. Firstly, UiO-66–NH_2 (Zr/Ce_x) with varying Ce doping ratios was solvothermally prepared (where "*x*" represents the mole ratio of the $CeCl_3$ added during synthesis). Subsequently, ligand deficiencies were introduced by means of pyrolysis under an argon atmosphere. Both pristine and defect-containing MOFs were characterized using X-ray diffraction (XRD) to examine the variations in their crystal structures (Fig. 1a, S2 and S3, in the ESI†). All samples exhibit high crystallinity and purity. UiO-66–NH_2 (Zr/Ce_x) displays XRD patterns similar to that of pristine its UiO-66–NH_2 counterpart, indicating the slight impact that the doped Ce has on the crystallographic features of the UiO-66–NH_2 framework.

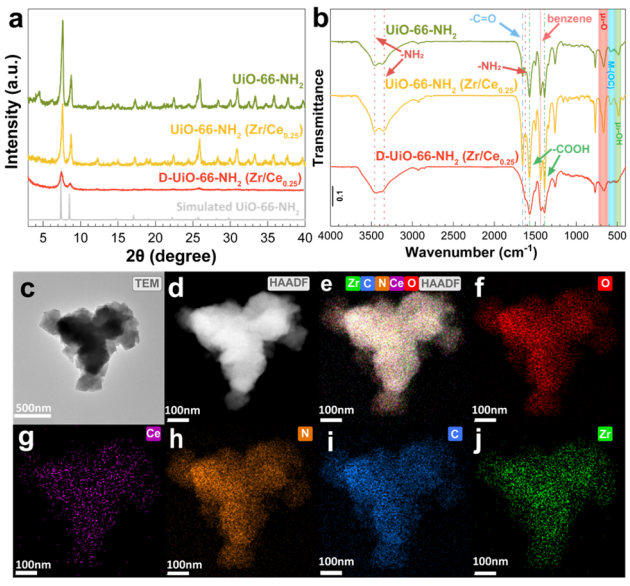

Fig. 1 (a) XRD patterns and (b) FT-IR spectra of D-UiO-66–NH_2 ($Zr/Ce_{0.25}$), UiO-66–NH_2 ($Zr/Ce_{0.25}$), UiO-66–NH_2, and simulated UiO-66–NH_2; (c) TEM image; (d) HAADF-STEM image; and (e–j) EDS mapping of D-UiO-66–NH_2 ($Zr/Ce_{0.25}$).

Regarding the form that Ce adopts in the clusters, previous studies reveal three available categories of cluster—$(Zr_6O_4(OH)_4$, $CeZr_5O_4(OH)_4$ and $Ce_6O_4(OH)_4$)—and only two of these can coexist.[26] Table S1† shows that the mole percentage of Ce in all the MOF samples is below 1/6. Under such circumstances, $Zr_6O_4(OH)_4$ and $CeZr_5O_4(OH)_4$ can coexist. $Ce_6O_4(OH)_4$ only forms when Ce addition exceeds 1/6.[26] As both Ce and Zr can both form $M_6O_4(OH)_4$ clusters, the substitution of Zr with Ce minimizes the impact on the XRD patterns of the final products, which is consistent with the experimental results in Fig. 1a. After pyrolysis, D-UiO-66–NH_2 ($Zr/Ce_{0.25}$) retains one broad peak at 2θ values of 7.4° and 8.6°, corresponding to the main peaks of UiO-66–NH_2, indicating that the framework and **fcu**-topology of UiO-66–NH_2 were maintained despite ligand loss. Further research indicated that if the $CeCl_3$ addition exceed 0.67, D-UiO-66–NH_2 ($Zr/Ce_{0.67}$) loses its framework structure (Fig. S4†).

Fig. 1b presents the Fourier-transform infrared (FT-IR) spectra of the as-prepared samples. Bands at 3460, 3343 and 1622 cm^{-1} are ascribed to the asymmetrical and symmetrical stretching vibrations of the free $-NH_2$ groups on the linkers.[27] Bands at 1571 and 1437 cm^{-1} correspond to the carboxylate and C–C bonds in the benzene ring skeleton.[28] The stretching vibration of C=O and the symmetrical vibration of the carboxylate are evident at 1656 and 1387 cm^{-1}, respectively.[29] Bands at 665 and 487 cm^{-1} are assigned to the M–O_{μ_3} and M–OH_{μ_3} stretching while the M–(OC) asymmetric stretching is observed at 565 cm^{-1}.[30] These observations confirm the coexistence and successful coordination of the $Zr_6O_4(OH)_4$ clusters and amino terephthalic acid in the samples. Furthermore, the FT-IR spectra of UiO-66–NH_2 (Zr/Ce_x) and D-UiO-66–NH_2 (Zr/Ce_x) exhibit similar bands (Fig. S5 and S6†), demonstrating their successful synthesis. Compared to UiO-66–NH_2 (Zr/Ce_x), D-UiO-66–NH_2 (Zr/Ce_x) shows broader and weaker bands corresponding to the –C=O, M–(OC) and M–OH_{μ_3} groups, providing evidence of ligand deficiencies and dihydroxylation of the Zr-oxo clusters.[31]

The morphology of UiO-66–NH_2 ($Zr/Ce_{0.25}$) and D-UiO-66–NH_2 ($Zr/Ce_{0.25}$) was analyzed using scanning electron microscopy (SEM) and transmission electron microscopy (TEM) (Fig. 1c and S7†). After pyrolysis, no significant morphological changes were observed, and D-UiO-66–NH_2 ($Zr/Ce_{0.25}$) retained a similar surface to that of UiO-66–NH_2 ($Zr/Ce_{0.25}$). High-resolution TEM (HRTEM) did not reveal distinct lattice fringes, suggesting that D-UiO-66–NH_2 ($Zr/Ce_{0.25}$) does not undergo transformation into cerium oxide or zirconium oxide agglomerates. High-angle annular dark-field scanning transmission electron microscopy (HAADF-STEM) and energy-dispersive spectroscopy (EDS) elemental mapping confirmed the uniform distribution of all elements (Fig. 1d–j).

Thermogravimetric analysis (TGA) under an air atmosphere and ^1H nuclear magnetic resonance (NMR) spectroscopy were employed to qualitatively and quantitatively assess the defect

levels. As shown in Fig. 2a, the number of remaining ligands in D-UiO-66–NH_2 (Zr/Ce_x) is significantly lower than in UiO-66–NH_2, indicating the successful introduction of ligand defects through pyrolysis. This finding is further supported by the quantitative ^{1}H NMR spectra. Generally, hydrofluoric acid is applied to digest the as-prepared samples while preserving the integrity of ligands. All digested samples show the same peaks (δ = 7.88, 7.43, 7.18) as a commercially available NH_2–H_2BDC sample (Fig. S8†). Notably, additional peaks appeared in the spectra of D-UiO-66–NH_2 (Zr/Ce_x) when compared to UiO-66–NH_2 (Zr/$Ce_{0.25}$) and pristine UiO-66–NH_2, which can be attributed to derivatives produced *via* the decarboxylation of NH_2–H_2BDC during pyrolysis (Fig. S9†).

By combining the ^{1}H NMR data with the inductively coupled plasma optical emission spectroscopy (ICP-OES) results, the ligand-to-cluster (L/C) ratios of the samples were determined (Table S2†). In ideal UiO-66, there are 12 dicarboxylate ligands coordinated to each $Zr_6O_4(OH)_4$ cluster with two clusters sharing one ligand, resulting in an L/C ratio of 6. For UiO-66–NH_2, the L/C ratio is measured to be 5.82, indicating the presence of minor ligand defects. Upon Ce^{III} doping, one of the 12 ligands (BDC–NH_2^{2-}) is expected to dissociate and compensate for the charge imbalance caused by Ce substitution. Consequently, the L/C ratio of UiO-66–NH_2 (Zr/$Ce_{0.25}$) decreases slightly to 5.71. After pyrolysis, the defect level of D-UiO-66–NH_2 (Zr/$Ce_{0.25}$) increased significantly, reducing the L/C ratio to 4.47, which is mainly attributed to the thermal treatment.

Site-selective linker removal

The selectively introduced defects originate from the coordination environment correlated thermal difference induced by Ce doping. Thus, it is rational to infer that the thermal properties of the MOFs will exhibit regular variation with increasing levels of cerium doping. The thermal stability of UiO-66–NH_2 (Zr/Ce_x) was characterized using TGA under a nitrogen atmosphere. Prior to TGA, all samples were immersed in a low boiling-point solvent (dichloromethane) and subjected to multiple solvent exchanges to completely remove the residual solvent from the pores. As illustrated in Fig. 2b, the stability of UiO-66–NH_2 (Zr/Ce_x) decreases with increasing levels of Ce doping. Differential thermogravimetry (DTG, Fig. 2c) reveals the distinct decomposition processes that occur. The first peak near 100 °C can be assigned to the evaporation of adsorbed water. Previous work reported that H_2BDC–NH_2 is a thermally labile ligand, and decarboxylation occurs between 300 and 400 °C in UiO-66–NH_2.[13] Therefore, the peak observed at around 300 °C can be assigned to ligand decarboxylation. Interestingly, a small additional peak near 200 °C is present in the DTG curves of UiO-66–NH_2 (Zr/$Ce_{0.25}$), UiO-66–NH_2 (Zr/$Ce_{0.28}$) and UiO-66–NH_2 (Zr/$Ce_{0.30}$). This peak is likely correlated to the cleavage of Ce–O_{COOH} or the decarboxylation of the ligands coordinated to Ce, indicating a localized structural impact from Ce doping.

In contrast, UiO-66–NH_2 and UiO-66–NH_2 (Zr/$Ce_{0.167}$), exhibit minimal cluster distortion and do not show significant pyrolysis below 300 °C. These findings further support the inference that the defect levels vary systematically with the Ce

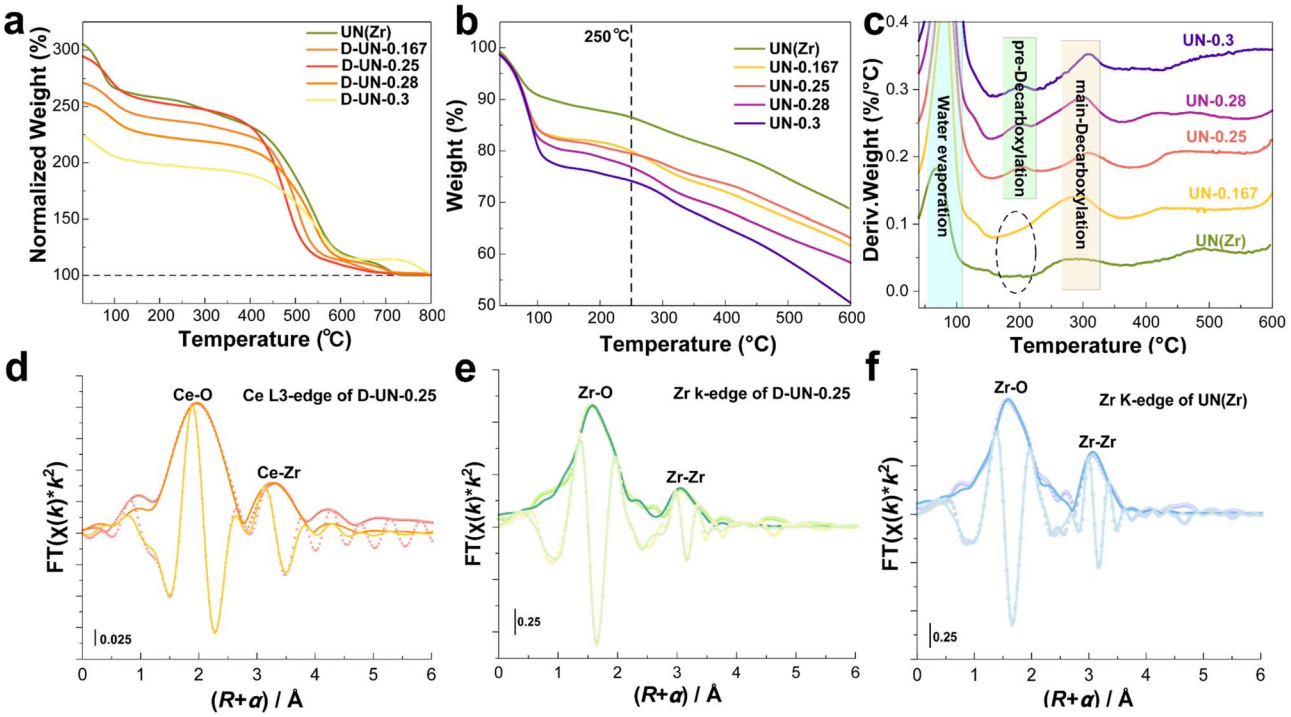

Fig. 2 (a) TGA of D-UiO-66–NH_2 (Zr/Ce_x) and UiO-66–NH_2 in air; (b) TGA and (c) DTG of UiO-66–NH_2 (Zr/Ce_x) and UiO-66–NH_2 in a N_2 atmosphere; (d and e) Ce L_3-edge, Zr K-edge EXAFS (points) and curve-fit (line) for D-UiO-66–NH_2 (Zr/$Ce_{0.25}$) shown in *R* space; (f) Zr K-edge EXAFS and curve-fit for UiO-66–NH_2 (FT magnitude and imaginary component). Data are k^2-weighted and not phase-corrected.

dosage. Quantitative ^{1}H NMR and ICP-OES data confirm that the L/C ratio of D-UiO-66–NH_2 (Zr/Ce_x) gradually decreases as the Ce dosage increases, consistent with the earlier assumption (Table S2†). In addition, ultraviolet-visible diffuse reflectance spectroscopy (UV-vis DRS) analysis of UiO-66–NH_2 (Zr/Ce_x) and D-UiO-66–NH_2 (Zr/Ce_x) reveals a similar trend (Fig. S10 and S11†). For UiO-66–NH_2 (Zr/Ce_x), the visible absorption expands with increasing cerium content, which can be ascribed to the level of Ce doping. The selectively introduced defects further enhance the impact of cerium on visible light absorption. The band gap shown in the Tauc plots also confirms this regular variation (Fig. S12 and S13†), indicating that the defect level in these materials is systematically modulated by the Ce dosage. Unlike the defect-containing MOFs induced by mixed ligands mentioned above, the ligands in UiO-66–NH_2 (Zr/Ce_x) are selectively removed not due to the intrinsic properties of the ligands, but due to their coordination environment.[25]

To further investigate the local coordination environment around Ce, EXAFS analysis was performed. Both wavelet transformation EXAFS (WT-EXAFS, Fig. S14–S16†) and Fourier-transform EXAFS (FT-EXAFS, Fig. 2d–f and S17–S19†) were applied. The peak at $R = 2.55$ Å is assigned to the Ce–O bonds in the ZrCe-oxo clusters and the peak at $R = 3.60$ Å is ascribed to the Ce–Zr distance (Fig. 2d and Table S3†). For the Zr K-edge of D-UiO-66–NH_2 (Zr/$Ce_{0.25}$) and UiO-66–NH_2, two paths Zr–O_{COOH} and Zr–O_{μ_3} are applied to fit the first shell, and the second shell is attributed to the Zr–Zr path (Fig. 2e, f, Tables S4 and S5†). The corresponding models are provided in Fig. S20–S22.†

FT-EXAFS fitting reveals a reduction in the coordination number (CN) of the Ce–O_{COO} bonds, as indicated by the low intensity of the corresponding peaks, which means all linkers around the Ce atoms are gone. Meanwhile, the CN of Zr–O_{COOH} for D-UiO-66–NH_2 (Zr/$Ce_{0.25}$) and UiO-66–NH_2 are 3.36 and 4, respectively (Tables S3–S5†). The CN of the Ce–O bonds is 2.63, which is significantly lower than that of Zr–O_{μ_3} in both D-UiO-66–NH_2 (Zr/$Ce_{0.25}$) and UiO-66–NH_2. In a typical $Zr_6O_4(OH)_4$ cluster, the Zr atoms are coordinated with $2O_{\mu_3}$, $2O_{\mu_3\text{-}OH}$ and 4 O_{COO}. Upon pyrolysis, $Zr_6O_4(OH)_4$ will lose two H_2O (derived from two $O_{\mu_3\text{-}OH}$ and four $H_{\mu_3\text{-}OH}$).[30] If it is assumed that $CeZr_5O_4(OH)_4$ loses either two $O_{\mu_3\text{-}OH}$ or loses nothing during pyrolysis, 68.5% of $CeZr_5O_4(OH)_4$ will give up two O atoms coordinated to Ce. Thus, the CN of Ce–O could decrease to 2.63 and the Ce-doped clusters turn into D (defect-containing)-ZrCe-oxo clusters. In conclusion, the FT-EXAFS analysis confirms that the Ce atoms lose all surrounding ligands and some O_{μ_3} during pyrolysis. The ligand defects are site-selectively introduced into D-UiO-66–NH_2 (Zr/$Ce_{0.25}$). Thus, by combining the EXAFS fitting and ligand quantification (Table S2†), we present a model in Fig. 3.

The Ce–O and Ce–Zr distances are longer than those of Zr–O and Zr–Zr due to the larger atomic radius of Ce. Such differences in atomic size lead to distortions in the clusters. Coupled with the weaker electrostatic interactions resulting from the lower valency of Ce^{III}, the linkers around Ce are prone to dissociate, thus explaining the origin of the selectively introduced defects.

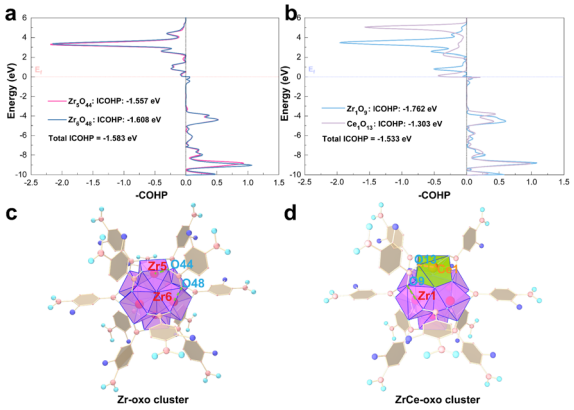

Fig. 3 COHP of (a) the Zr-oxo clusters and (b) the ZrCe-oxo clusters; models of (c) the Zr-oxo clusters and (d) the ZrCe-oxo clusters.

To elucidate the origin of selectively introduced defects from a theoretical perspective, crystal orbital Hamilton population (COHP) calculations were conducted to evaluate the strength of the M–OC bonds between the linkers and metals (Fig. 3). Generally, a negative integrated COHP value indicates the formation of a chemical bond and a higher absolute value corresponds to stronger bonds. Obviously, the Ce_1–O_{13} bond in the ZrCe-oxo clusters is weaker than the Zr–O bond in the Zr-oxo clusters. Though the Zr_1–O_9 bond in ZrCe-oxo is stronger, the total integrated COHP values of Ce_1–O_{13} and Zr_1–O_9 in the CeZr-oxo clusters still indicate a weaker interaction compared with the two Zr–O bonds in the Zr-oxo clusters. As a result, there is a lower energy barrier for the ligands coordinated with Ce to dissociate. As a consequence, the selective defect engineering creates D-ZrCe-oxo clusters with an unsymmetrical pyramid. The top of the pyramid is a Ce atom and the base consists of four Zr atoms.

Photocatalytic performance

To investigate the impact of the selectively introduced defects on photocatalytic performance, we conducted CO_2 photoreduction experiments. An online gas detection system (Perfectlight Labsolar 6A) was applied to assess the photocatalytic performance of the as-prepared samples under mild conditions (300 W Xe lamp with an AM 1.5G filter and a water-cooling system at 25 °C). The performance of D-UiO-66–NH_2 (Zr/Ce_x) was assessed (Fig. S23†). Carbon monoxide is the only gas product. The products in water was also tested with ^{1}H NMR, and no liquid products could be detected (Fig. S24†). With increasing Ce doping, the performance of D-UiO-66–NH_2 (Zr/Ce_x) shows a volcano-shaped trend, which is ascribed to the effect of the increase in the defect levels and structural collapse. Compared to pristine UiO-66–NH_2, UiO-66–NH_2 (Zr/$Ce_{0.25}$) shows a slight improvement while D-UiO-66–NH_2 (Zr/$Ce_{0.25}$) exhibits the best performance, approximately 2.4 times that of UiO-66–NH_2 (Fig. 4a). To elucidate whether the enhanced performance originates from Ce doping, linker defects, or their synergistic effects, we employed two distinct defect engineering approaches to synthesize UiO-66 with linker defects. The first

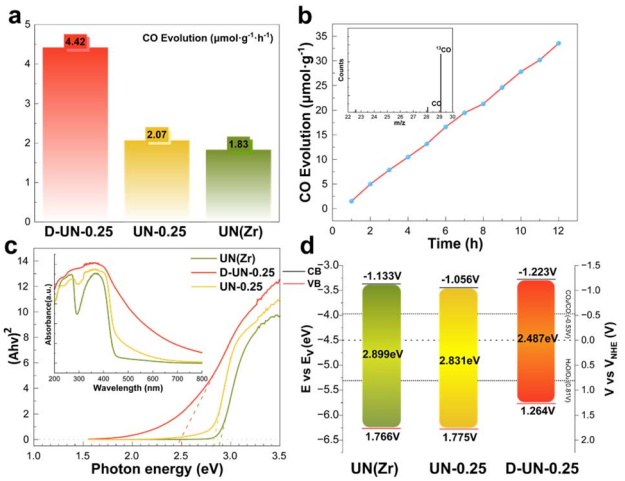

Fig. 4 (a) CO evolution rate of D-UiO-66–NH_2 (Zr/$Ce_{0.25}$), UiO-66–NH_2 (Zr/$Ce_{0.25}$) and UiO-66–NH_2; (b) stability of D-UiO-66–NH_2 (Zr/$Ce_{0.25}$) and $^{13}CO_2$ labelling experiment (inset); (c) Tauc plot and UV-vis DRS spectra (inset) and (d) band structure of UiO-66–NH_2, UiO-66–NH_2 (Zr/$Ce_{0.25}$), and D-UiO-66–NH_2 (Zr/$Ce_{0.25}$).

approach, designated as D-UiO-66–NH_2-x (where x denotes the addition of acetic acid), utilized a modulator-assisted defect strategy. The second approach employed a mixed-linker (ML) strategy to selectively induce linker defects, as described in the Introduction. The resulting materials were designated as D-ML-UiO-66(y), where y indicates the molar ratio of amino terephthalate to terephthalate. Their structure and defect concentrations were characterized using XRD (Fig. S25–S27†) and quantified *via* ^{1}H NMR spectroscopy (Table S2†). As shown in Fig. S28,† none of the modified samples exceeded the performance of D-UiO-66–NH_2 (Zr/$Ce_{0.25}$), demonstrating the synergistic enhancement achieved through the synergy of Ce doping and site-selective defect engineering.

To verify the photocatalytic stability of D-UiO-66–NH_2 (Zr/$Ce_{0.25}$), we conducted 12 h continuous photocatalytic experiments. D-UiO-66–NH_2 (Zr/$Ce_{0.25}$) maintains a steady CO_2 photoreduction rate as shown in Fig. 4b, demonstrating high stability under irradiation for a long time period. Furthermore, TEM and XRD analysis of D-UiO-66–NH_2 (Zr/$Ce_{0.25}$) after 12 h of irradiation shows negligible changes, indicating good stability (Fig. S29 and S30†). ^{1}H NMR quantitative defect level characterization also confirms that the L/C ratio shows a negligible decrease (Table S2†). No substantial CO was detected in control experiments without illumination and catalysts. To confirm the carbon source of the generated CO, an isotope labelling experiment was conducted by replacing CO_2 with $^{13}CO_2$ during the photocatalysis. As shown in the inset of Fig. 4b, it is clear that ^{13}CO ($m/z = 29$) is the dominant product, indicating that the CO mainly originated from CO_2 photoreduction instead of decomposition of the ligands or other sources. The high stability of the photocatalyst can be assigned to strong Zr–O bonds and high coordination number of the $Zr_6O_4(OH)_4$ clusters.[32]

We systematically compared our results with recently reported photocatalytic performances of defect-containing MOFs (Table S6†). The comparison reveals that most reported MOF-based systems rely on unsustainable photosensitizers and organic sacrificial agents. In contrast, this work focuses on enhancing the intrinsic photocatalytic activity of UiO-66–NH_2 without requiring additional photosensitizers or sacrificial agents.

Photocatalysis mechanism

Photocatalysis can be divided into three fundamental processes: light absorption and excitation of electrons, charge separation and migration, and surface redox reactions. The light absorption capacity of the as-prepared samples was characterized using UV-vis DRS (Fig. 4c). Band gaps were calculated using the Kubelka–Munk function and the results are listed in Table S7.† Pristine UiO-66–NH_2 exhibits the broadest band gap and doping with Ce narrows the band gap to 2.831 eV (UiO-66–NH_2 (Zr/$Ce_{0.25}$)). After pyrolysis, D-UiO-66–NH_2 (Zr/$Ce_{0.25}$) has an even narrower band gap of 2.487 eV. To further unveil the band structure, Mott–Schottky analysis was conducted to calculate the flat band potential (V_{fb}) to evaluate the conduction band (CB) potential (Fig. S31–S33†). All the as-synthesized samples exhibit a positive slope, indicating they are all n-type semiconductors and the bottom of the CB is 0.1–0.3 eV lower than the V_{fb}. Thus, the V_{CB} and V_{VB} (potentials of the conduction band and valence band) can be determined and a band structure diagram is plotted in Fig. 4d. As shown in Fig. 4d, all samples have more negative V_{CB} than the reduction potential of (CO_2/CO) while they have more positive V_{VB} than the oxidation potential of (H_2O/O_2). From a thermodynamic perspective, all the samples can finish the oxidation and reduction half-reactions.

Furthermore, density of state (DOS) calculations were performed to elucidate the mechanism responsible for the band variations (Fig. S34†). The band gap of the Zr-oxo-clusters is calculated as 0.126 eV while the D-ZrCe-oxo clusters do not have a band gap. Obviously, the projected DOS of Ce contribute greatly to the total DOS (TDOS) and crosses the Fermi level, and thus the bandgap is significantly narrowed. Moreover, Ce doping and the selectively introduced defects change the coordination environment of Zr. Zr contributes to the TDOS and expands the lowest unoccupied crystal orbits. Although the bandgap energy is underestimated by the restricted calculation method, the trend remains in the results obtained from the Tauc plots.

During carrier separation and migration, recombination is inevitable and significantly reduces photocatalytic performance. To investigate the charge separation and migration efficiency, photoelectrochemical experiments were conducted. Electrochemical impedance spectroscopy (EIS) Nyquist plots (Fig. 5a) reveal that D-UiO-66–NH_2 (Zr/$Ce_{0.25}$) exhibits the smallest semicircle diameter, indicating minimal resistance to carrier migration. The photocurrent responses (Fig. 5b) demonstrate that D-UiO-66–NH_2 (Zr/$Ce_{0.25}$) has the highest photocurrent, suggesting that it has the most efficient charge separation and migration of all the samples.

Photoluminescence (PL) emission spectroscopy and time-resolved photoluminescence (TRPL) spectroscopy were

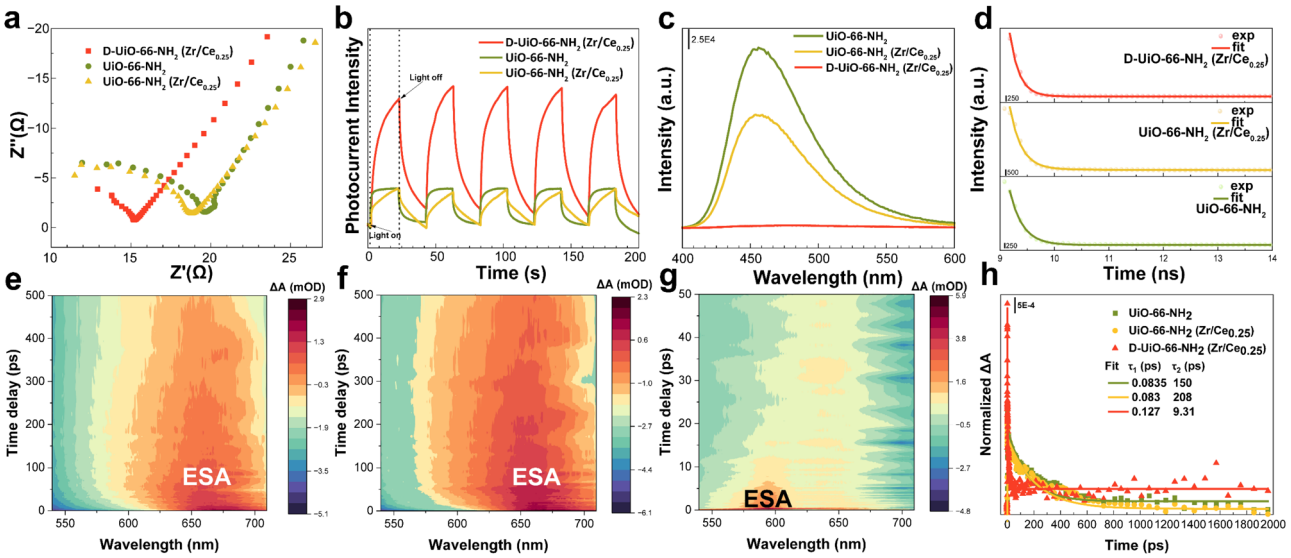

Fig. 5 (a) EIS, (b) photocurrent response, (c) PL, and (d) TRPL of UiO-66–NH_2, UiO-66–NH_2 (Zr/$Ce_{0.25}$) and D-UiO-66–NH_2 (Zr/$Ce_{0.25}$); fs-TAS of (e) UiO-66–NH_2, (f) UiO-66–NH_2 (Zr/$Ce_{0.25}$) and (g) D-UiO-66–NH_2 (Zr/$Ce_{0.25}$); (h) TAS decay kinetics were monitored at 663.6 nm for UiO-66–NH_2 and UiO-66–NH_2 (Zr/$Ce_{0.25}$) and at 592.6 nm for D-UiO-66–NH_2 (Zr/$Ce_{0.25}$).

performed to evaluate the charge recombination. In Fig. 5c, UiO-66–NH_2 exhibits the highest photoluminescence intensity at 460 nm, while D-UiO-66–NH_2 (Zr/$Ce_{0.25}$) shows negligible PL emission near 480 nm. A lower PL intensity indicates reduced carrier recombination in D-UiO-66–NH_2 (Zr/$Ce_{0.25}$). This finding is further supported by the TRPL results (Fig. 5d). The average fluorescence lifetime (τ) is calculated using the following equation:

$$\tau = (B_1\tau_1^2 + B_2\tau_2^2 + B_3\tau_3^2)/(B_1\tau_1 + B_2\tau_2 + B_3\tau_3)$$

where τ_1, τ_2, and τ_3 represent the fluorescent lifetimes and B_1, B_2, and B_3 represent the amplitudes. All statistics are listed in Table S8 (ESI†). The τ value of UiO-66–NH_2 is calculated to be 0.237 ns, while that of UiO-66–NH_2 (Zr/$Ce_{0.25}$) is 0.422 ns. Meanwhile, the site-selective defect engineering shortens the lifetime of D-UiO-66–NH_2 (Zr/$Ce_{0.25}$) to 0.173 ns, suggesting enhanced charge separation and suppressed exciton recombination.[33]

To further explore the charge transfer, femtosecond transient absorption spectroscopy (fs-TAS) was conducted. As is demonstrated in Fig. 5e–g, UiO-66–NH_2 and UiO-66–NH_2 (Zr/$Ce_{0.25}$) show broad positive features at 640–700 nm. These positive features can be ascribed to excited-state absorption (ESA) induced by charge transfer and charge separation.[34] LCCT (ligand to cluster charge transfer) might be the main cause of the signal at 640–700 nm.[35] However, D-UiO-66–NH_2 (Zr/$Ce_{0.25}$) only shows a slightly positive signal at 640–700 nm while it demonstrates a stronger positive signal at 590 nm. Obviously, the ESA signal of D-UiO-66–NH_2 (Zr/$Ce_{0.25}$) undergoes a faster dynamics process within 20 ps while it takes approximate 100 ps for the ESA signals of UiO-66–NH_2 and UiO-66–NH_2 (Zr/$Ce_{0.25}$) to vanish. Consistent with the TRPL, the TAS kinetics also demonstrate that D-UiO-66–NH_2 (Zr/$Ce_{0.25}$) has the shortest lifetime, further confirming the faster decay of the ESA signal of D-UiO-66–NH_2 (Zr/$Ce_{0.25}$) (Fig. 5h). These observations suggest that D-UiO-66–NH_2 (Zr/$Ce_{0.25}$) displays weak LCCT because of the loss of ligands. Meanwhile, another stronger electron transfer pathway is opened up and induces faster charge separation and transfer.

XPS was applied to analyze the surface states of UiO-66–NH_2 (Zr/$Ce_{0.25}$) and D-UiO-66–NH_2 (Zr/$Ce_{0.25}$). XPS confirms the presence of C, N, O, Zr, and Ce in both samples (Fig. S35†). In Fig. S36 and Table S9,† the Zr 3d spectrum of D-UiO-66–NH_2 (Zr/$Ce_{0.25}$) revealed that the Zr $3d_{5/2}$ and $3d_{3/2}$ peaks appear at 182.47 and 184.88 eV, corresponding to the Zr^{IV} oxidation state.[36] Meanwhile, the Ce 3d spectrum (Fig. S37 and Table S8†) of D-UiO-66–NH_2 (Zr/$Ce_{0.25}$) displays two peaks at 886.74 and 882.46 eV for Ce $3d_{5/2}$ and two peaks at 905.41 and 901.10 eV for Ce $3d_{3/2}$, confirming the presence of Ce^{III}.[37] Interestingly, compared with UiO-66–NH_2 (Zr/$Ce_{0.25}$), the Zr 3d peaks of D-UiO-66–NH_2 (Zr/$Ce_{0.25}$) are shifted to a lower binding energy (BE) while the Ce 3d peaks are shifted to a higher BE. These findings indicate that Zr is partially reduced, while Ce is partially oxidized, with a similar shift in magnitude of approximately 0.6 eV for both elements, thus suggesting that an electron transfer path exists between Ce and Zr.[38] In photocatalysis, Zr acts as a reduction site, while the Ce serves as an oxidation site. The Ce L_3-edge XANES spectra of UiO-66–NH_2 (Zr/$Ce_{0.25}$) and D-UiO-66–NH_2 (Zr/$Ce_{0.25}$) reveal their bulk oxidation states (Fig. S38†). Both materials exhibit Ce(III) signatures, while UiO-66–NH_2 (Zr/$Ce_{0.25}$) additionally shows a characteristic Ce(IV) peak at 5738 eV, indicating mixed-valence states.[39] We propose a Ce(III)-terminated surface with bulk Ce(III)/Ce(IV) mixed valence in UiO-66–NH_2 (Zr/$Ce_{0.25}$). This phenomenon has been documented previously,[40] where formic acid addition during synthesis suppresses Ce(III) oxidation to Ce(IV).[40] On the one hand, monocarboxylic acid can introduce linker defects, whilst

on the other hand, the surface of UiO-66–NH_2 is usually capped by monocarboxylic acid or water, which can also be seen as a linker defect state. As a result, we attribute the Ce(IV) → Ce(III) transformation (Fig. S39†) during pyrolysis to linker deficiency-induced stabilization of the Ce(III) state. Ce(IV) reduction creates a Zr–Ce charge imbalance, facilitating Zr–O–Ce electron transfer pathways.

To verify this electron transfer mechanism, we performed *ex situ* XPS measurements under dark and illuminated conditions (Fig. 6a, b and Table S10†). High-resolution Zr 3d and Ce 3d spectra were acquired for D-UiO-66–NH_2 (Zr/$Ce_{0.25}$) under both conditions. The peaks of Zr 3d shift to lower BE, while the peaks of Ce 3d shift to higher BE compared with the results obtained in darkness. To further understand the electron transfer pathway, the O 1s spectrum was obtained and is displayed in Fig. 6c and Table S11.† The ZrCe-oxo clusters and Zr-oxo-clusters both have three typical oxygen species: carboxyl oxygen, μ_3-O and μ_3-OH. Therefore, the spectrum of UiO-66–NH_2 (Zr/$Ce_{0.25}$) was deconvoluted into three peaks. However, a new peak at 533.87 eV, attributed to uncoordinated carboxyl oxygen, appears in the spectrum of D-UiO-66–NH_2 (Zr/$Ce_{0.25}$).[38] Obviously, the proportion of μ_3-O increases while that of carboxyl oxygen reduces in the change from UiO-66–NH_2 (Zr/$Ce_{0.25}$) to D-UiO-66–NH_2 (Zr/$Ce_{0.25}$), indeed, massive linker defects result in this case.

However, because water is adsorbed in the form of –OH, the proportion of M-μ_3-OH only decreases from 23.4% to 12.2%. In contrast, the BE of μ_3-O shows the reverse tendency, indicating an increase in the electron density in D-UiO-66–NH_2 (Zr/$Ce_{0.25}$). Interestingly, the BE shift of μ_3-O between UiO-66–NH_2 (Zr/$Ce_{0.25}$) and D-UiO-66–NH_2 (Zr/$Ce_{0.25}$) is merely −0.21 eV, which might be due to the effect of the electron transfer pathway.

Both Ce and Zr exist in UiO-66–NH_2 (Zr/$Ce_{0.25}$) and D-UiO-66–NH_2 (Zr/$Ce_{0.25}$). However, the electron transfer pathway is closed up before the site-selective defect engineering is conducted. To further investigate the pathway, electron paramagnetic resonance (EPR) spectroscopy was conducted. As depicted in Fig. 6d, a sharp and symmetrical peak at $g = 2.003$ is ascribed to the unpaired electrons trapped by the O vacancies while a peak at $g = 2.021$ indicates the existence of Zr^{3+} species.[41–43] Furthermore, Ce L_3-edge EXAFS fitting of D-UiO-66–NH_2 (Zr/$Ce_{0.25}$) suggests a significantly lower coordination number for the Ce–O path compared to the Zr-oxo clusters. This finding indicates that the μ_3-oxygen atoms near Ce in the ZrCe-oxo clusters are partially lost during pyrolysis, leading to the formation of numerous oxygen vacancies. This could explain why D-UiO-66–NH_2 (Zr/$Ce_{0.25}$) exhibits the most intense EPR signal. Based on these observations, we can further infer that the trapped electrons do not localize evenly between Ce and Zr due to their different valencies. Instead, the trapped electrons prefer the Zr atoms. Upon illumination, the excited electrons transfer from Zr to the adsorbed CO_2, and then the trapped electrons will transfer to Zr, promoting charge separation. To identify the critical intermediates during the photoreduction, *in situ* diffuse reflection infrared Fourier-transform spectroscopy (DRIFTS) was conducted. As shown in Fig. 6e, after aerating CO_2 into the system, the spectrum has obvious CO_2 asymmetric stretching peaks (2340 cm^{-1}, Fig. S39†), confirming CO_2 adsorption.[15] There exist few peaks corresponding to intermediates until illumination occurs. The peaks at 1664 and 1483 cm^{-1} are correlated to bicarbonate (HCO_3^-).[44] The peak corresponding to bidentate carbonate (b-CO_3^{2-}) is found at 1593 cm^{-1}.[45] Most importantly, the peaks at 1550 and 1200 cm^{-1} provide strong evidence for the presence of critical intermediate *COOH.[46] Based on this spectrum, we propose the following mechanism for the photocatalytic conversion of CO_2 to CO:

$$CO_2(g) \rightarrow *CO_2$$

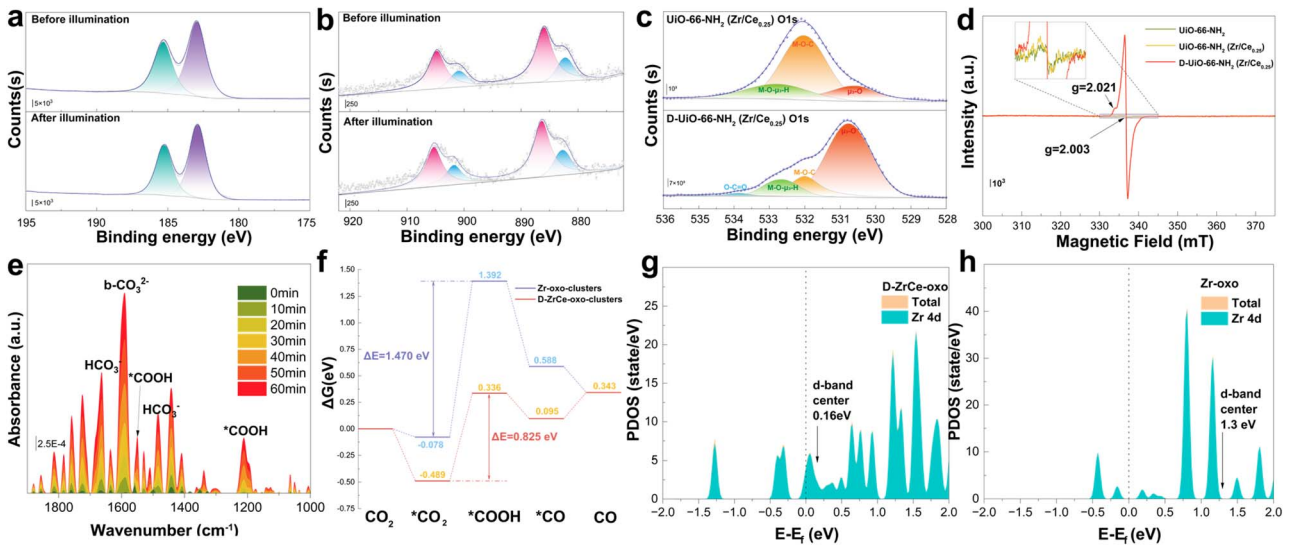

Fig. 6 *Ex situ* XPS fine spectroscopy results for (a) Zr 3d and (b) Ce 3d in D-UiO-66–NH_2 (Zr/$Ce_{0.25}$); (c) XPS fine spectroscopy results for O 1s in UiO-66–NH_2 (Zr/$Ce_{0.25}$) and D-UiO-66–NH_2 (Zr/$Ce_{0.25}$); (d) EPR signal of UiO-66–NH_2, UiO-66–NH_2 (Zr/$Ce_{0.25}$) and D-UiO-66–NH_2 (Zr/$Ce_{0.25}$); (e) *in situ* FTIR spectrum of D-UiO-66–NH_2 (Zr/$Ce_{0.25}$); (f) Gibbs free energy profiles for CO_2 photoreduction on Zr-oxo clusters and the D-ZrCe-oxo clusters; PDOS of (g) D-ZrCe-oxo and (h) Zr-oxo.

$$H_2O \rightarrow H^+ + OH^-$$

$$*CO_2 + e^- + H^+ \rightarrow *COOH$$

$$*COOH + e^- + H^+ \rightarrow *CO + H_2O$$

$$*CO \rightarrow CO(g)$$

where "*" means molecules adsorbed on the catalyst surface.[46] A mechanism is also shown in Fig. S40.† Charge density difference, Bader charge analysis and Gibbs free energy profiles were calculated to reveal the electron transfer pathway and variation in thermodynamics during the photoreaction procedure. Fig. 6f demonstrates that both clusters have a positive adsorption energy (eV), suggesting spontaneous CO_2 adsorption. However, due to the loss of the surrounding linkers, the D-ZrCe-oxo-clusters can adsorb CO_2 with less steric hindrance and exhibit higher adsorption energy. Moreover, due to the proximity of Ce to Zr, two oxygen atoms from CO_2 can coordinate simultaneously with Ce and Zr, thus promoting CO_2 adsorption. More importantly, the D-ZrCe-oxo-clusters show a significantly lower energy barrier at the rate-determining step ($*CO_2 + e^- + H^+ \rightarrow *COOH$), which can be attributed to electron accumulation at Zr, as evidenced by the XPS and EPR results. The PDOS of Zr 4d and the d-band center were also calculated for two clusters.

Notably, after selective defect engineering, the Zr 4d-orbitals redistribute and the d-band center of Zr 4d drops from 1.3 to 0.16 eV, indicating that the latter has better catalytic performance (Fig. 6g and h).[47,48] Charge density difference and Bader charge analysis also give similar results whereby the Zr in the Zr-oxo-clusters only transfers 0.004 and 0.131 electrons to $*CO_2$ and *COOH, respectively. Meanwhile, the Zr in the D-ZrCe-oxo clusters transfers 1.304 and 0.768 electrons to $*CO_2$ and *COOH, respectively, indicating higher activity for the Zr in the D-ZrCe-oxo-clusters (Fig. S41 and S42†).

Therefore, we propose the following mechanism: according to a "LCCT" mechanism, upon irradiation, electrons are injected from the amino terephthalic acid moieties to the clusters.[35] Simultaneously, electrons in the metal-oxo-clusters can be excited. However, the Zr-oxo-cluster with 12 linkers is highly symmetrical, and therefore, the injected electrons are likely to recombine with the holes left in the clusters. Conversely, linkers with selectively introduced defects give the D-ZrCe-oxo-clusters an unsymmetrical pyramidal structure. The Ce atoms located at the top of pyramid cannot receive electrons from the linkers but act as the accumulation sites of the holes. The excited electrons can transfer through the Ce–O–Zr and Ce–$O_{vacancy}$–Zr pathways to Zr, realizing spatial charge separation. Finally, the adsorbed CO_2 and H_2O is reduced and oxidized to finish the photoreaction.

Conclusions

In this work, we prepared Ce-doped UiO-66–NH_2 (Zr/Ce_x) with site-selective linker defects using a method which leverages differences in the coordination environment. Linkers coordinated with Ce are prone to leaving under pyrolysis and induce the formation of site-selective defects. First, Ce doping narrows the band gap then improves the photoabsorption. Furthermore, the site-selective defects further induce the formation of unsymmetrical clusters with a pyramidal architecture and reduce Ce(IV) to Ce(III). A charge imbalance between the Ce(III) and Zr(IV) opens up a Zr–Ce electron transfer pathway, promoting electrons to accumulate at the Zr and the holes at the Ce, thus facilitating spatial charge separation and suppressing charge recombination. The exposed Zr and Ce sites favour the adsorption of CO_2 and H_2O for CO_2 photoreduction without the use of any organic sacrificial agents. A 2.4 times improvement in photocatalytic performance was achieved by D-UiO-66–NH_2 (Zr/$Ce_{0.25}$). This work may provide meaningful perspectives for future research on defect-containing MOFs.

Data availability

The data supporting this article have been included as part of the ESI.†

Author contributions

Yuhang Qi conceived the idea. Yuhang Qi, Fanchao Meng, and Shiyu Wang performed the experiments and analyzed the synthesis, reactivity and characterization data. Yuhang Qi the manuscript wrote and Yiqiang He, Yuxin Liu, Zhe Zhang, Chunguang Li, Xiaobo Chen, Zhan Shi, and Shouhua Feng edited the manuscript.

Conflicts of interest

There are no conflicts to declare.

Acknowledgements

This work was financially supported by the National Natural Science Foundation of China (22271114), '111 Center' (B17020) and by the program for JLU Science and Technology Innovative Research Team (JLUSTIRT). The authors are grateful to the professional support from beamline BL13SSW, BL11B and BL17B1 at the Shanghai Synchrotron Radiation Facility. The authors extend their gratitude to Theoretical and Computational Chemistry Team from Scientific Compass (**https://www.shiyanjia.com**) for providing invaluable assistance.

Notes and references

1 A. Li, Q. Cao, G. Y. Zhou, B. Schmidt, W. J. Zhu, X. T. Yuan, H. L. Huo, J. L. Gong and M. Antonietti, Three-Phase Photocatalysis for the Enhanced Selectivity and Activity of CO_2 Reduction on a Hydrophobic Surface, *Angew. Chem., Int. Ed.*, 2019, **58**, 14549–14555.

2 Y. Wang, Z. Y. Zhang, J. Li, Y. W. Yuan, J. Yang, W. Xu, P. F. An, S. B. Xi, J. P. Guo, B. Liu and J. F. Li, Two-Dimensional-on-Three-Dimensional Metal-Organic Frameworks for Photocatalytic H_2 Production, *Angew. Chem., Int. Ed.*, 2022, **61**, 9.

3 C. X. Zhang, C. F. Xie, Y. Y. Gao, X. P. Tao, C. M. Ding, F. T. Fan and H. L. Jiang, Charge Separation by Creating Band Bending in Metal-Organic Frameworks for Improved Photocatalytic Hydrogen Evolution, *Angew. Chem., Int. Ed.*, 2022, **61**, 6.

4 J. D. Xiao, L. L. Han, J. Luo, S. H. Yu and H. L. Jiang, Integration of Plasmonic Effects and Schottky Junctions into Metal-Organic Framework Composites: Steering Charge Flow for Enhanced Visible-Light Photocatalysis, *Angew. Chem., Int. Ed.*, 2018, **57**, 1103–1107.

5 X. Z. Fang, Q. C. Shang, Y. Wang, L. Jiao, T. Yao, Y. F. Li, Q. Zhang, Y. Luo and H. L. Jiang, Single Pt Atoms Confined into a Metal-Organic Framework for Efficient Photocatalysis, *Adv. Mater.*, 2018, **30**, 7.

6 J.-D. Xiao, R. Li and H.-L. Jiang, Metal–Organic Framework-Based Photocatalysis for Solar Fuel Production, *Small Methods*, 2023, **7**, 2201258.

7 N. Liu, B. Hu, K. Tang, T. Xia, F. Li, G. Quan, X. Zhang and L. Tang, Assembling UiO-66 into layered HTiNbO5 nanosheets for efficient photocatalytic CO2 reduction, *Surf. Interfaces*, 2023, **41**, 103134.

8 N. Liu, K. Tang, D. Wang, F. Fei, H. Cui, F. Li, J. Lei, D. Crawshaw, X. Zhang and L. Tang, Enhanced photocatalytic CO2 reduction by integrating an iron based metal-organic framework and a photosensitizer, *Sep. Purif. Technol.*, 2024, **332**, 125873.

9 W. Huang, Z. Zhang, J. Xu, H. Cui, K. Tang, D. Crawshaw, J. Wu, X. Zhang, L. Tang and N. Liu, Highly Selective CO2 Conversion to CH4 by a N-Doped HTiNbO5/NH2-UiO-66 Photocatalyst without a Sacrificial Electron Donor, *JACS Au*, 2025, **5**, 1184–1195.

10 Z. X. Sun, K. Sun, M. L. Gao, Ö. Metin and H. L. Jiang, Optimizing Pt Electronic States through Formation of a Schottky Junction on Non-reducible Metal-Organic Frameworks for Enhanced Photocatalysis, *Angew. Chem., Int. Ed.*, 2022, **61**, e202206108.

11 S. Guo, L.-H. Kong, P. Wang, S. Yao, T.-B. Lu and Z.-M. Zhang, Switching Excited State Distribution of Metal–Organic Framework for Dramatically Boosting Photocatalysis, *Angew. Chem., Int. Ed.*, 2022, **61**, e202206193.

12 H.-L. Zheng, J.-Q. Zhao, Y.-Y. Sun, A.-A. Zhang, Y.-J. Cheng, L. He, X. Bu, J. Zhang and Q. Lin, Multilevel-Regulated Metal–Organic Framework Platform Integrating Pore Space Partition and Open-Metal Sites for Enhanced CO2 Photoreduction to CO with Nearly 100% Selectivity, *J. Am. Chem. Soc.*, 2023, **145**, 27728–27739.

13 L. Feng, S. Yuan, L.-L. Zhang, K. Tan, J.-L. Li, A. Kirchon, L.-M. Liu, P. Zhang, Y. Han, Y. J. Chabal and H.-C. Zhou, Creating Hierarchical Pores by Controlled Linker Thermolysis in Multivariate Metal–Organic Frameworks, *J. Am. Chem. Soc.*, 2018, **140**, 2363–2372.

14 X. Feng, H. S. Jena, C. Krishnaraj, D. Arenas-Esteban, K. Leus, G. B. Wang, J. M. Sun, M. Rüscher, J. Timoshenko, B. R. Cuenya, S. Bals and P. Van der Voort, Creation of Exclusive Artificial Cluster Defects by Selective Metal Removal in the (Zn, Zr) Mixed-Metal UiO-66, *J. Am. Chem. Soc.*, 2021, **143**, 21511–21518.

15 Y. He, C. Li, X.-B. Chen, Z. Shi and S. Feng, Visible-Light-Responsive UiO-66(Zr) with Defects Efficiently Promoting Photocatalytic CO2 Reduction, *ACS Appl. Mater. Interfaces*, 2022, **14**, 28977–28984.

16 M. Li, Y. Liu, F. Li, C. Shen, Y. V. Kaneti, Y. Yamauchi, B. Yuliarto, B. Chen and C.-C. Wang, Defect-Rich Hierarchical Porous UiO-66(Zr) for Tunable Phosphate Removal, *Environ. Sci. Technol.*, 2021, **55**, 13209–13218.

17 S. Bai, N. Zhang, C. Gao and Y. J. Xiong, Defect engineering in photocatalytic materials, *Nano Energy*, 2018, **53**, 296–336.

18 Z. Ai, L. Jiao, J. Wang and H.-L. Jiang, Generation of Hierarchical Pores in Metal–Organic Frameworks by Introducing Rigid Modulator, *CCS Chem.*, 2022, **4**, 3705–3714.

19 M. Taddei, G. M. Schukraft, M. E. A. Warwick, D. Tiana, M. J. McPherson, D. R. Jones and C. Petit, Band gap modulation in zirconium-based metal-organic frameworks by defect engineering, *J. Mater. Chem. A*, 2019, **7**, 23781–23786.

20 Y. He, Y. Liu, C. Chen, X. Wang, C. Li, X.-B. Chen, Z. Shi and S. Feng, Defect-Induced All-Solid-State Frustrated Lewis Pair on Metal–Organic Monolayer Accelerating Photocatalytic CO2 Reduction with H2O Vapor, *Nano Lett.*, 2024, **24**, 5047–5056.

21 Z. Lei, Y. Xue, W. Chen, W. Qiu, Y. Zhang, S. Horike and L. Tang, MOFs-Based Heterogeneous Catalysts: New Opportunities for Energy-Related CO2 Conversion, *Adv. Energy Mater.*, 2018, **8**, 1801587.

22 Z. Wang, X. Yue and Q. Xiang, MOFs-based S-scheme heterojunction photocatalysts, *Coord. Chem. Rev.*, 2024, **504**, 215674.

23 C. Liu, H. R. Q. Liu, J. C. Yu, L. Wu and Z. H. Li, Strategies to engineer metal-organic frameworks for efficient photocatalysis, *Chin. J. Catal.*, 2023, **55**, 1–19.

24 S. Sk, H. Islam, B. M. Abraham, I. Mondal and U. Pal, Defects in MOFs for Photocatalytic Water Reduction to Hydrogen Generation: From Fundamental Understanding to State-of-Art Materials, *Small Methods*, 2024, DOI: **10.1002/smtd.202401689**.

25 S. Naghdi, A. Cherevan, A. Giesriegl, R. Guillet-Nicolas, S. Biswas, T. Gupta, J. Wang, T. Haunold, B. C. Bayer, G. Rupprechter, M. C. Toroker, F. Kleitz and D. Eder, Selective ligand removal to improve accessibility of active sites in hierarchical MOFs for heterogeneous photocatalysis, *Nat. Commun.*, 2022, **13**, 282.

26 K. A. Lomachenko, J. Jacobsen, A. L. Bugaev, C. Atzori, F. Bonino, S. Bordiga, N. Stock and C. Lamberti, Exact Stoichiometry of CexZr6–x Cornerstones in Mixed-Metal UiO-66 Metal–Organic Frameworks Revealed by Extended X-ray Absorption Fine Structure Spectroscopy, *J. Am. Chem. Soc.*, 2018, **140**, 17379–17383.

27 J. J. Pan, L. J. Wang, Y. X. Shi, L. L. Li, Z. Xu, H. R. Sun, F. Guo and W. L. Shi, Construction of nanodiamonds/UiO-66-NH_2 heterojunction for boosted visible-light photocatalytic degradation of antibiotics, *Sep. Purif. Technol.*, 2022, **284**, 10.

28 J. Guo, X. Fan, J. Wang, S. Yu, M. Laipan, X. Ren, C. Zhang, L. Zhang and Y. Li, Highly efficient and selective recovery of

Au(III) from aqueous solution by bisthiourea immobilized UiO-66-NH2: performance and mechanisms, *Chem. Eng. J.*, 2021, **425**, 130588.

29 M. Lammert, M. T. Wharmby, S. Smolders, B. Bueken, A. Lieb, K. A. Lomachenko, D. De Vos and N. Stock, Cerium-based metal organic frameworks with UiO-66 architecture: synthesis, properties and redox catalytic activity, *Chem. Commun.*, 2015, **51**, 12578–12581.

30 L. Valenzano, B. Civalleri, S. Chavan, S. Bordiga, M. H. Nilsen, S. Jakobsen, K. P. Lillerud and C. Lamberti, Disclosing the Complex Structure of UiO-66 Metal Organic Framework: A Synergic Combination of Experiment and Theory, *Chem. Mater.*, 2011, **23**, 1700–1718.

31 J.-J. Duan, X. Xin, S.-J. Guo, S.-L. Wang, H. Chen, J.-L. Li, S. Qin and G.-H. Tao, Regulating defected zirconium metal–organic frameworks in ionic liquid for sewage treatment, *J. Mol. Struct.*, 2023, **1286**, 135607.

32 R. M. Rego, M. D. Kurkuri and M. Kigga, A comprehensive review on water remediation using UiO-66 MOFs and their derivatives, *Chemosphere*, 2022, **302**, 22.

33 C. Cheng, J. J. Zhang, B. C. Zhu, G. J. Liang, L. Y. Zhang and J. G. Yu, Verifying the Charge-Transfer Mechanism in S-Scheme Heterojunctions Using Femtosecond Transient Absorption Spectroscopy, *Angew. Chem., Int. Ed.*, 2023, **62**, 8.

34 Y. Xiao, Q. Sun, J. Leng and S. Jin, Time-Resolved Spectroscopy for Dynamic Investigation of Photoresponsive Metal–Organic Frameworks, *J. Phys. Chem. Lett.*, 2024, **15**, 3390–3403.

35 Y. Isaka, Y. Kawase, Y. Kuwahara, K. Mori and H. Yamashita, Two-Phase System Utilizing Hydrophobic Metal-Organic Frameworks (MOFs) for Photocatalytic Synthesis of Hydrogen Peroxide, *Angew. Chem., Int. Ed.*, 2019, **58**, 5402–5406.

36 A. K. Kar, R. Sarkar, A. K. Manal, R. Kumar, S. Chakraborty, R. Ahuja and R. Srivastava, Unveiling and understanding the remarkable enhancement in the catalytic activity by the defect creation in UIO-66 during the catalytic transfer hydrodeoxygenation of vanillin with isopropanol, *Appl. Catal., B*, 2023, **325**, 15.

37 P. Liu, P. Jing, X. Xu, B. Liu and J. Zhang, Structural Reconstruction of Ce-MOF with Active Sites for Efficient Electrocatalytic N2 Reduction, *ACS Appl. Energy Mater.*, 2021, **4**, 12128–12136.

38 H. H. He, J. P. Yuan, P. Y. Cai, K. Y. Wang, L. Feng, A. Kirchon, J. Li, L. L. Zhang, H. C. Zhou and Y. Fang, Yolk-Shell and Hollow Zr/Ce-UiO-66 for Manipulating Selectivity in Tandem Reactions and Photoreactions, *J. Am. Chem. Soc.*, 2023, **145**, 17164–17175.

39 H. Yoshida, L. Yuliati, T. Hamajima and T. Hattori, Valence of Highly Dispersed Cerium Oxide Species on Silica Quantitatively Estimated by Ce L_{III}-edge XANES, *Mater. Trans.*, 2004, **45**, 2062–2067.

40 M. Ronda-Lloret, I. Pellicer-Carreño, A. Grau-Atienza, R. Boada, S. Diaz-Moreno, J. Narciso-Romero, J. C. Serrano-Ruiz, A. Sepúlveda-Escribano and E. V. Ramos-Fernandez, Mixed-Valence Ce/Zr Metal-Organic Frameworks: Controlling the Oxidation State of Cerium in One-Pot Synthesis Approach, *Adv. Funct. Mater.*, 2021, **31**, 2102582.

41 T. R. Gordon, M. Cargnello, T. Paik, F. Mangolini, R. T. Weber, P. Fornasiero and C. B. Murray, Nonaqueous Synthesis of TiO2 Nanocrystals Using TiF4 to Engineer Morphology, Oxygen Vacancy Concentration, and Photocatalytic Activity, *J. Am. Chem. Soc.*, 2012, **134**, 6751–6761.

42 I. Nakamura, N. Negishi, S. Kutsuna, T. Ihara, S. Sugihara and K. Takeuchi, Role of oxygen vacancy in the plasma-treated TiO2 photocatalyst with visible light activity for NO removal, *J. Mol. Catal. A: Chem.*, 2000, **161**, 205–212.

43 S.-Q. Wang, X. Wang, X.-M. Cheng, J. Ma and W.-Y. Sun, Tailoring defect-type and ligand-vacancies in Zr(iv) frameworks for CO2 photoreduction, *J. Mater. Chem. A*, 2022, **10**, 16396–16402.

44 C.-C. Yang, Y.-H. Yu, B. van der Linden, J. C. S. Wu and G. Mul, Artificial Photosynthesis over Crystalline TiO2-Based Catalysts: Fact or Fiction?, *J. Am. Chem. Soc.*, 2010, **132**, 8398–8406.

45 H. Yu, F. Chen, X. Li, H. Huang, Q. Zhang, S. Su, K. Wang, E. Mao, B. Mei, G. Mul, T. Ma and Y. Zhang, Synergy of ferroelectric polarization and oxygen vacancy to promote CO2 photoreduction, *Nat. Commun.*, 2021, **12**, 4594.

46 X. Jiao, X. Li, X. Jin, Y. Sun, J. Xu, L. Liang, H. Ju, J. Zhu, Y. Pan, W. Yan, Y. Lin and Y. Xie, Partially Oxidized SnS2 Atomic Layers Achieving Efficient Visible-Light-Driven CO2 Reduction, *J. Am. Chem. Soc.*, 2017, **139**, 18044–18051.

47 L. Ju, X. Tan, X. Mao, Y. Gu, S. Smith, A. Du, Z. Chen, C. Chen and L. Kou, Controllable CO2 electrocatalytic reduction via ferroelectric switching on single atom anchored In2Se3 monolayer, *Nat. Commun.*, 2021, **12**, 5128.

48 Z. Zhang, Z. Zhang, M. Xie, R. Tian, C. Chai, R. Xu, X.-b. Chen, Y. Song, H. Lu, Z. Shi and S. Feng, Enhancing Oxygen Reduction Reaction through Asymmetric Electronic Structure-Mediated d-π Interaction, *CCS Chem.*, 2025, **7**, 867–882.